Automatic in-situ radiometric calibration for mobile laser scanning: Compensating for distance and angle of incidence effects

Helena Laasch[1], Tomislav Medic[1], Andreas Wieser[1]

[1] Institute of Geodesy and Photogrammetry, ETH Zürich, 8000 Zurich, Switzerland - (laaschh, tmedic, wiesera)@ethz.ch

Keywords: LiDAR, Mobile Laser Scanning, Intensity, Radiometric Calibration, Remote Sensing, Segmentation.

Abstract

Laser scanner intensity data provide valuable insights into material properties, enabling applications such as point cloud segmentation and material probing. However, extracting meaningful information is challenging due to the influence of the measurement configuration represented by the angle of incidence (AOI) and distance. Although existing methods for radiometric calibration in terrestrial laser scanning (TLS) exist, they rely on either overlapping scans from discrete positions or on manual segmentation. This limits their applicability to mobile laser scanning (MLS), which typically produces very large datasets (requiring automation) with little or no overlap, and from continuously changing positions. This study presents an approach for adapting an automatic in-situ radiometric calibration method originally developed for TLS that applies to MLS. Building on our previous work, we introduce techniques to estimate AOI and distance influence compensation functions with little or without overlap, as well as non-discrete scan stations, and propose two strategies for AOI influence compensation - global and local. The global method computes one best-fitting AOI compensation function for the entire scan. It uses local reflectance estimation, which relies on a modified filtering technique, accommodating the unique characteristics of MLS data. The local method computes the best-fitting AOI compensation function per segment, ideally containing a single material. We use machine learning for point cloud semantic segmentation with additional instance segmentation to automatically obtain a material proxy segment. We evaluate the proposed methods on four datasets captured by two different MLS systems, demonstrating their ability to reduce measurement configuration related influences on intensities and enhance following point cloud segmentation.

1. Introduction

Laser scanners commonly record the intensity of the backscattered signal as an auxiliary measurement. This intensity can be related to material properties and used in various applications, e.g., point cloud segmentation and material probing (Harintaka and Wijaya, 2024; Li et al., 2024; Maru et al., 2023; Viswanath et al., 2023; Pfreundschuh et al., 2024; Han et al., 2022; Jin et al., 2021; Tan et al., 2020; Kaasalainen et al., 2010). However, retrieving the material information from the recorded intensity is not trivial, as measurement configuration related influences and other effects overlay this information (Pfeifer et al., 2008). Therefore, mitigating these effects is necessary to fully leverage the intensities for downstream tasks and, consequently, numerous studies (e.g., Kashani et al. (2015), Sanchiz-Viel et al. (2021)) have focused on understanding these effects and developed methods to model and isolate them.

In terrestrial and mobile laser scanning (TLS and MLS), the impact of the measurement configuration, represented by the angle of incidence (AOI) and distance, has been identified as the primary influence. Investigating and modeling the relationship between intensity and measurement configuration was initially tackled over a decade ago (e.g., Kaasalainen et al. (2005), and Pfeifer et al. (2007)). However, all methods available until now require additional calibration scans or manual segmentation of areas with uniform surface and material properties. Furthermore, most methods were designed for specific applications and datasets, limited to only a few targets with different properties (often only one type).

Our recent study introduced a method for automatic in-situ radiometric calibration of TLS intensity (Laasch et al., 2025). This method compensates for the measurement configuration globally using one best-fitting AOI and one distance compensation function for the entire point cloud, initially disregarding the material-dependent characteristics of the AOI function. To account for this deficiency, we demonstrated how the method can be additionally adapted to estimate local material-dependent AOI compensation. Both of these approaches (global and local) are not directly transferable to MLS data, as they rely on overlapping scans from multiple discrete scan stations. Motivated by the increasing use of MLS, in this study we adapted both the global and the local approach to accommodate the specific requirements of MLS data. The proposed methods are evaluated on four datasets captured by two different MLS systems, demonstrating their ability to reduce measurement configuration related influences on intensities and to enhance following point cloud segmentation.

The remainder of this paper is structured as follows: Sec. 2 provides the theoretical background, explaining the physical principles behind intensity and their relationship to material reflectance coefficients. Sec. 3 describes the original method and the necessary adaptations for MLS. In Sec. 4, we present the datasets used for evaluation. Sec. 5 discusses the results obtained with the adapted method. Finally, Sec. 6 concludes the paper with a summary of findings and potential future research directions.

2. Theoretical Background

The LiDAR equation (Jelalian, 1992) establishes a relationship between the received and emitted power by considering various influencing factors. Among these is the measurement configuration, an aspect this work seeks to model and address. The

LiDAR equation can be expressed as follows:

$$P_r = \frac{P_e D_r^2}{4\pi \beta_e^2 R^4} \frac{4\pi A\rho}{\Omega} \eta_{\text{Atm}} \eta_{\text{Sys}} + P_{\text{BR}}. \tag{1}$$

Here, P_r is the received power, P_e the emitted power P_e, D_r the receiving aperture diameter, β_e the beam divergence, R the distance to the target surface, A the illuminated area, ρ the reflection coefficient of the target surface, Ω the scattering solid angle of the target surface, η_{Atm} the atmospheric transmission, η_{Sys} the system transmission, and P_{BR} the background radiation.

For MLS, as with TLS, several simplifying assumptions can be applied, as, e.g., done in Laasch et al. (2025). This includes the assumptions that: (i) the target surface is significantly larger than the laser beam width, allowing the illuminated area to be approximated as $A = R^2\beta_e^2\frac{\pi}{4}$, and (ii) atmospheric transmission and background radiation are negligible. Furthermore, most instruments do not directly output the received power; instead, they assign an intensity value to each point in the point cloud. The relationship between intensity and the received power can be linear, logarithmic, or more complex. In this study we use the linear model as we validate our method on MLS systems using Zoller+Fröhlich instruments for which we have the confirmation by the manufacturer that the intensity-power relationship is linear. By applying these simplifications, Eq. 1 can be transformed into

$$I^s_{\text{r},j,k} = \frac{\gamma P_e D_r^2 \eta^s_{R_0}}{4} \cdot \frac{\pi}{\Omega^{\text{mat}_j}_{\varphi_0}} \cdot \frac{\eta^s_R}{R^2} \cdot \rho^{\text{mat}_j}_{\varphi_0}, \tag{2}$$

where $I^s_{\text{r},j,k}$ is the intensity of point j measured from position k using the scanner s, γ is the linear scale of the intensity vs. power relationship, $\eta^s_{R_0}$ is the distance-independent part of the system transmission at the reference distance R_0, and η^s_R is the distance-dependent part. Additionally, ρ_{φ_0} refers to the reflection coefficient at the reference AOI φ_0, and Ω_{φ_0} is the AOI-dependent scattering solid angle of the target surface for φ_0. More information about the individual components can be found, e.g. in our previous work Laasch et al. (2025). What is relevant for this work is that each part of Eq. 2 can be expressed as either a constant or a function. These functions are separable, as they depend on different variables, allowing their independent estimation. This can be expressed as:

$$I^s_{\text{r},j,k} = \kappa^s_{R_0} \cdot f^{\text{mat}_j}_{\varphi_0}(\varphi_{j,k}) \cdot g^s_{R_0}(R_{j,k}) \cdot \rho^{\text{mat}_j}_{\varphi_0}, \tag{3}$$

where:

- $\kappa^s_{R_0}$ is a constant specific to the scanner s and an arbitrarily chosen reference distance R_0.
- $f^{\text{mat}_j}_{\varphi_0}(\varphi_{j,k})$ describes AOI-dependent effects on intensity, and depends on the target's material properties mat_j, the AOI $\varphi_{j,k}$, and an arbitrarily chosen reference AOI φ_0.
- $g^s_{R_0}(R_{j,k})$ describes the distance-dependent effects and depends on the scanner s, the distance between the measured point and scanner position, and on R_0.
- $\rho^{\text{mat}_j}_{\varphi_0}$ represents the reflection coefficient at φ_0 determined by the target's material properties mat_j.

In an ideal scenario, the terms $\kappa^s_{R_0}$, $f^{\text{mat}_j}_{\varphi_0}(\varphi_{j,k})$ and $g^s_{R_0}(R_{j,k})$ can be estimated or are known, allowing $\rho^{\text{mat}_j}_{\varphi_0}$ to be calculated. However, in most practical cases, the system constant $\kappa^s_{R_0}$ is unknown. Consequently, $\kappa^s_{R_0}$ and $\rho^{\text{mat}_j}_{\varphi_0}$ can only be estimated as a combined term. Following the approach of Laasch et al. (2025), we refer to this combination as measurement configuration independent intensity $I^s_{\text{MCI},j,k}$:

$$I^s_{\text{MCI},j,k} = \kappa^s_{R_0} \cdot \rho^{\text{mat}_j}_{\varphi_0}. \tag{4}$$

The derived term $I^s_{\text{MCI},j,k}$ depends on the scanner and is neither an exact nor a necessarily complete quantification of the material's reflection properties ($f^{\text{mat}_j}_{\varphi_0}(\varphi_{j,k})$ also depends on the material). However, it is independent of the measurement configuration and, hence, a valuable parameter for applications like i) improving point cloud segmentation by facilitating the differentiation of target materials and surfaces, and ii) monitoring the changes in material properties (e.g., wetness) over time from different viewpoints. In the following text, we briefly describe the method for estimating $I^s_{\text{MCI},j,k}$ for TLS data that we introduced in our previous work (Laasch et al., 2025), and subsequently, we elaborate on changes done within this study to adapt the method for MLS data.

3. Methods

3.1 TLS method

The original method by Laasch et al. (2025) for TLS comprises three stages: Point cloud preprocessing, Cycle 1, and Cycle 2 (see Fig. 1). The point cloud preprocessing stage consists of three steps. In the first step, essential parameters such as distance and AOI are computed for each point in the point cloud. In the second step, each point is assigned a neighborhood patch defined by a spherical region with a predefined radius (we used 10 cm, experimentally defined). The radius must be sufficiently large to ensure an adequate number of points per patch while remaining small enough to maintain the assumption of consistent reflectance within the patch. Finally, in the third step, the point cloud is filtered based on criteria such as surface variation (i.e. roughness), maximal scanning distance, and the number of different scan stations present within a neighborhood patch. Cycle 1 involves iteratively estimating the AOI $f^{\text{mat}_j}_{\varphi_0}(\varphi_{j,k})$ and distance $g^s_{R_0}(R_{j,k})$ compensation functions relying on the least-squares best-fit of smoothing splines. The process takes iteratively improved ("compensated") intensities as the input, bins them with a pre-defined number of bins over the entire range of AOI or distance values, computes bin averages and uses them as data points in the fitting procedure for computing $f^{\text{mat}_j}_{\varphi_0}(\varphi_{j,k})$, and $g^s_{R_0}(R_{j,k})$. Cycle 2 includes Cycle 1 with additionally iteratively estimating reflectance normalization values. These values are used to "correct" the intensity values, which helps to iteratively improve Cycle 1 estimates (explanation follows).

The primary focus of the original work was on such global compensation with reflectance normalization, in which a single AOI compensation function is estimated for the entire dataset. This process leverages the scan overlaps of multiple scan stations to obtain iteratively refined reflectance estimates by averaging the continuously "compensated" intensities of multiple point clouds within neighborhood patches. These reflectance estimates are used as normalization coefficients applied to all related points. This approach mitigates bias in modeling the relationship between the intensity and the measurement configuration when the best-fit functions are estimated using the entire heterogeneous point cloud. This forms the foundation for radiometric calibration. The reflectance estimation assumes: (i) neighboring points measured from different scan stations have similar reflectance normalization values, (ii) sufficient variation in distances and AOIs exist within the predefined neighborhoods, and it allows for decoupling of all relevant variables and prevents misinterpreting these effects as reflectance variations.

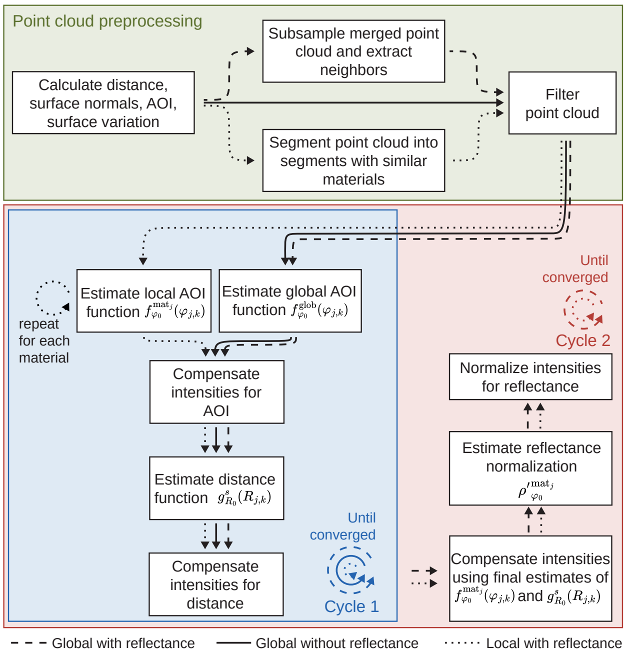

Figure 1. The original method by Laasch et al. (2025) for automatic in-situ radiometric calibration, complemented with adaptations for MLS data.

Moreover, in our previous work, we demonstrated the improved radiometric calibration when the function modeling intensity-AOI relationship was locally adapted for each material (see dotted lines in Fig. 1). However, for that demonstration, we relied on manually segmenting point clouds into segments with uniform material properties. Further information about the approach and implementation for TLS can be found in Laasch et al. (2025).

Adaptations for MLS are required since the method relies on overlapping point clouds from multiple scan stations, which are absent in MLS data. Additionally, we aim to avoid manual segmentation by using a machine learning-based point cloud semantic segmentation combined with instance segmentation.

3.2 Adaptation of the method for MLS

To adapt the method of Laasch et al. (2025) for MLS data, it is necessary to account for the lack of discrete scan stations and the reduced or no point cloud overlap. These differences in the data affect the filtering of the point cloud and the estimation of the reflectance normalization values, which are required to ensure unbiased AOI and distance compensation functions estimates. Various approaches can be used to adapt the original method for MLS data. We have developed three, suited for different datasets and applications, which are described in more detail in the following paragraphs.

Global without reflectance estimation: A straightforward approach is by bypassing reflectance normalization (the only step that explicitly relies on scans with high overlap taken from discrete stations), and not filtering with the number of scan stations present within a neighborhood patch (see solid lines in Fig. 1). In this case, estimating distance and AOI compensation functions relies on the assumption of uniform distribution of average reflectance coefficients across the bins of distance and AOI values (see Sec. 3.1). This assumption is debatable, especially for typical MLS datasets. For instance, a car-mounted MLS predominantly scans road surfaces at short distances, where lane markings may appear predominantly within a limited number of AOI and distance bins. Hence, the average reflectance, and therefore intensity within these bins will be notably off from the remaining values used in the fitting procedure, which can bias the function estimates. Nonetheless, we implemented this method, tested its efficiency, and evaluated the impact of non-uniformly distributed reflectance coefficients.

Global with reflectance estimation: This approach follows the original method described by Laasch et al. (2025), including the neighborhood patch extraction (see dashed lines in Fig. 1). However, the filtering step is modified since MLS data lacks discrete scan stations. In the original method, the patches are filtered based on the number of different scan stations contributing to a patch. For MLS data, we instead calculate the spread of distance and AOI values within each patch, defined as the difference between the 99th and 1st percentiles of the distance and AOI values. Patches with a spread below a certain manually defined threshold are excluded.

This modified filtering process ensures that the remaining patches have sufficient variation in AOI and distance, which reduces the coupling of these variables with the estimated reflectance normalization values. However, there is a trade-off when choosing the threshold values. Although choosing the smaller spread thresholds increases the risk of inadvertently compensating for AOI or distance effects rather than the reflectance, choosing the larger thresholds reduces the number of available patches, which can also negatively affect the estimation of the AOI and distance compensation function. Hence, these threshold parameters have to be selected with care based on some prior knowledge about the dataset.

Local with reflectance estimation: To improve the precision of the radiometric compensation, instead of estimating one best-fit AOI compensation function for the entire point cloud, disregarding different behavior of different materials, in this implementation, we estimate multiple locally best-fitting AOI compensation functions (see dotted lines in Fig. 1). Ideally, this requires segmentation of all point cloud points by common material. However, we found no readily available algorithm for such a segmentation that works effectively with our dataset. Hence, to at least get a proxy for the material in an automated way, we adopted a machine learning model (Road 1.0, a model implemented in Leica Cyclone 3DR software) that performs object-related semantic segmentation. This model classifies point cloud points into classes such as buildings, road surfaces, vegetation, and curbstones. Here, our assumption is that the points related to a common semantic class are more likely to share similar material properties and, hence, would require a similar AOI compensation function.

To further improve the results, we additionally performed instance segmentation within each semantic class to separate individual objects, since some classes, such as buildings, consist of multiple objects that may not share the same surface characteristics and material properties. For this step, we used the DB-

Scan algorithm (Ester et al., 1996), and we additionally merged all instances with fewer than a certain number of points (we used 2’000, experimentally defined) to ensure sufficient data for estimating the AOI and distance compensation functions. Apart from the described adjustment in creating the correspondences between data points and the appropriate $f_{\varphi_0}^{\mathrm{mat}_j}(\varphi_{j,k})$ functions, the algorithm remains unchanged from the original method.

4. Datasets

To evaluate our method, we used four different MLS datasets. Tab. 1 provides an overview of these datasets. Datasets 1 to 3 were acquired using an MLS system mounted on a handcart and consisting of a single 2d profiling laser scanner tilted by -30° in the pitch direction, a surveying-grade GNSS receiver, and a navigation-grade IMU. Dataset 4 was captured using an MLS system mounted on a car. This system included two laser scanners of the same type, tilted by -30° in pitch direction and additionally by $\pm 45^\circ$ in yaw direction, a GNSS receiver and an IMU of comparable quality to the previous MLS system.

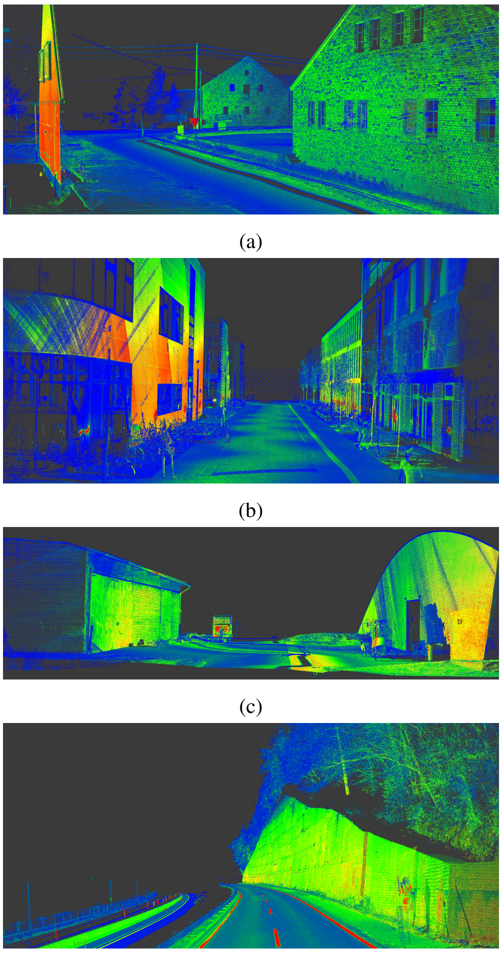

(a) (b) (c) (d)

Figure 2. Point clouds of the provided datasets colored by the raw intensity: (a) Dataset 1, (b) Dataset 2, (c) Dataset 3, and (d) Dataset 4.

None of the datasets were captured under ideal conditions for radiometric calibration. Rather than adapting the data acquisition process, we chose to test the methods on existing datasets to evaluate their applicability under unmodified normal working conditions. For instance, an ideal dataset would involve capturing the same objects from various positions with different distances and AOIs. This could be achieved by including rotational maneuvers in the trajectories or conducting multiple drives from different viewpoints. Among the datasets, only Dataset 4 includes multiple drives over the same location. However, the drives were recorded along very similar trajectories, introducing small additional distribution of AOI and distance values. Specifically, the car traversed the same street twice in both directions, resulting in two almost identical trajectories. The two trajectory pairs are also similar, as they lie approximately 4 m apart (small range of values relative to the instrument’s measurement range of 119 m).

For each dataset, the trajectory of the MLS system was extracted from a Kalman-filter-based navigation solution relying on the acquired IMU and GNSS data (using software that was either in-house developed by the respective research groups or provided by the MLS system manufacturer). Using the timestamps associated with each point cloud point and expressed in a common time with the trajectory data (GPS time), we linearly interpolated the trajectories to compute the scanner’s positions at the time of each point acquisition. This positional information allowed us to calculate the distance and AOI for each point.

The intensity data were exported differently across the datasets. For Datasets 1 to 3, intensity values were provided as raw intensity, whereas for Dataset 4, they were exported as reflectance values, which are pre-compensated for distance by the manufacturer. Using the intensity values, along with the computed distance and AOI, it is possible to estimate the distance and AOI compensation functions. The following section presents the results of the compensation applied to these four datasets.

5. Results

In this section, we present the performance of the methods presented in Sec. 3 on the previously introduced datasets. Visual evaluation is demonstrated using an exemplary part of a retaining wall from Dataset 4 using the global method with reflectance estimation (see Fig. 3). The other datasets and methods show comparable results. The related point cloud is colored once with raw intensities (see Fig. 3b) and once using the estimated $I^s_{\mathrm{MCI},j,k}$ (see Fig. 3c). Fig. 3b, which visualizes raw intensity, reveals a gradient in intensity values from the top to the bottom. This gradient arises because the distance and AOI values decrease from the top to the bottom. In contrast, Fig. 3c, where $I^s_{\mathrm{MCI},j,k}$ is used, does not exhibit this gradient. Thus, the implemented method successfully reduces the impact of the measurement configuration. As a consequence, differences in material properties within the wall segment become evident, allowing for eventual segmentation based on the intensity values (demonstration follows).

Furthermore, to quantitatively evaluate the results of the proposed radiometric calibration methods, we defined distinct homogeneous areas within the scenes for analysis. In each dataset, 6 to 10 such areas were selected, each approximately 3 m long and 1 m wide. This selection ensures that each area encompasses a range of distances and AOIs. Within these areas, all points are expected to have the same or very similar $I^s_{\mathrm{MCI},j,k}$ values, resulting in a small spread of values. Hence, by analyzing the distribution of uncorrected intensities and $I^s_{\mathrm{MCI},j,k}$ values within these areas, we derived a statistical metric to assess the performance of our method. Specifically, we considered the

Dataset	Scanners	# points [$\cdot 10^6$]	# Drives	Scenery	Source
1	1 Z+F Profiler 9012A	18	1	Rural village (houses, street, meadow)	Heinz (2021)
2	1 Z+F Profiler 9012A	47	1	University campus (houses with shiny facades, street)	Heinz (2021)
3	1 Z+F Profiler 9012A	23	1	Farm (large concrete wall, barn, meadow, paved floor)	Heinz (2021)
4	2 Z+F Profiler 9012	160	4	Overland road (road, retaining wall)	Kalenjuk et al. (2021)

Table 1. Overview of used datasets to evaluate the proposed methods.

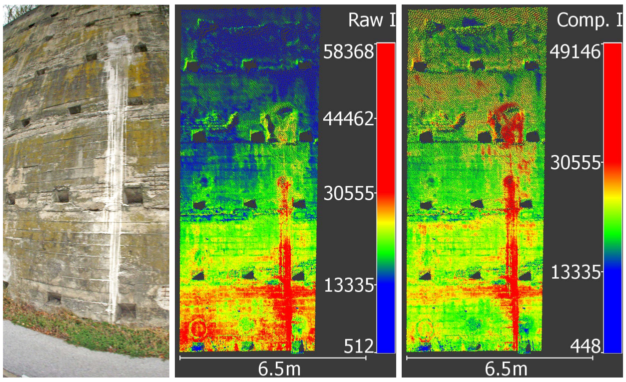

(a) (b) (c)

Figure 3. Part of an almost vertical retaining wall of Dataset 4 shown as RGB image (a) and the corresponding point cloud colored with the raw intensity (b) and the $I^{s}_{\mathrm{MCI},j,k}$ (c).

coefficient of variation (CV). The CV is a standard measure for assessing variability and is defined as the ratio of the standard deviation to the mean of all values (intensities).

This metric was calculated for each selected area in each dataset and then averaged within the datasets to produce a single representative value per dataset. The metrics for each dataset are shown in Tab. 2. It presents the three methods illustrated in Fig. 1, and the local method is applied twice: first using the instances obtained from the segmentation (see Sec. 3.2) and then using the classes without instance segmentation. For each dataset, one single distance compensation function is estimated, even if the dataset contains multiple scanners from the same type (e.g., Dataset 4).

Method		Dataset 1	2	3	4
Raw		0.25	0.47	0.47	0.22
Global	With refl.	**0.16**	0.28	0.18	**0.19**
	Without refl.	0.19	0.23	0.18	0.27
Local	Classes	0.20	**0.21**	0.17	0.24
	Instances	0.18	0.25	**0.15**	0.22

Table 2. CV of radiometric calibration. The best metrics are in bold and blue, whereas the worst metrics are in red.

For the global methods, the metrics in Dataset 1-3 show a decrease compared to the one calculated from raw intensities. This indicates that both global methods can achieve, to a certain degree, a radiometric compensation regardless of whether they use reflectance estimation or not.

However, in Dataset 4, improved metrics are only observed when reflectance estimation is incorporated. The worse value observed for the method without reflectance estimation can be attributed to the presence of some highly reflective objects in Dataset 4 consistently measured at similar distances and AOIs, see e.g. the lane marking example in Sec. 3.2 (see Fig. 2d). This consistency creates a bias in the estimation of the distance and AOI compensation functions and subsequently negatively affects the radiometric calibration results.

In contrast, the improved value in Dataset 4 for the method with reflectance estimation, relative to the without case, is achieved partially due to the availability of multiple scanning trajectories. These trajectories lead to sufficient variations in distance and AOI values for the same objects, which enables the calculation of the reflectance normalization values with sufficient quality. Consequently, the addition of reflectance estimation successfully reduces the bias due to the large differences in the reflectivity of the objects used for distance and AOI compensation functions.

The metrics discussed so far are calculated using the entire Dataset 4, which contains data collected from two scanners (see Tab. 1). When these metrics are calculated separately for each scanner, they match those obtained for the entire dataset, indicating that both scanners share comparable distance compensation functions. We compare the distance functions because we assume that the AOI compensation functions are scanner-independent and only dependent on the scanned objects.

To further assess whether separate distance compensation function estimations are necessary for each scanner, Fig. 4 depicts the distance compensation functions estimated for the right, left, and combined data from both scanners. Although some artifacts are noticeable at short distances and beyond 20 m, likely due to the non-uniform distribution of averaged reflectance values (see Sec. 3), the estimated functions exhibit similar shapes, likely indicating no significant differences. However, confirming this hypothesis would require further analysis. Additionally, we would expect the distance compensation functions to be smoother. The observed artifacts may result from an insufficient number of data points in these regions and/or an overly weak smoothness constraint in the spline approximations. A more in-depth investigation would be necessary to fully understand these effects. However, such an ablation study is beyond the scope of this work.

If we include the distance function estimated using the combined Dataset 1-3 – where all three datasets are merged to minimize the influence of non-uniformly distributed reflectance values – we can better observe the difference between the manufacturer's distance-compensated intensities (Dataset 4) and the raw intensities (Dataset 1-3). This demonstrates that the adapted method effectively handles both cases and reduces the impact of measurement configuration. However, in the already distance-compensated intensities functions, a deviation remains between the estimated function and the manufacturer's compensation function. Otherwise, the estimated function would be a straight line. Further investigation is needed to determine whether this deviation results from systematic effects in the applied method or from additional adaptations, as the manufacturer's function may not generalize perfectly to all scenes.

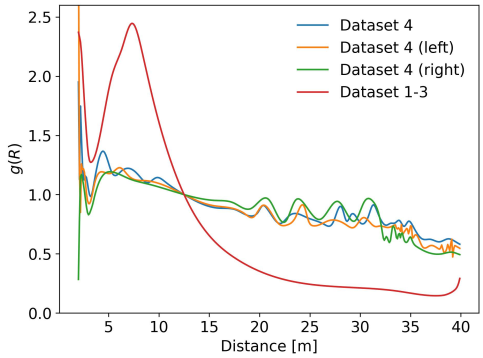

Figure 4. Distance compensation function estimated with Dataset 4 both scanners together, with only the right or left scanner and with the combined Dataset 1-3.

Compared to the global methods, the local methods yield improved metrics for Datasets 2 and 3. This is due to the advantage of locally adapted AOI compensation functions, which assign distinct compensation functions to segments with similar radiometric properties, allowing for better modeling of material-specific radiometric behavior. However, the drawback is the smaller quantity of data available for estimating AOI compensation functions per segment, which can reduce estimation accuracy.

In Dataset 2, the segmentation process enhances the estimation of $I^s_{\mathrm{MCI},j,k}$, leading to improved metrics (see Table 2). This dataset contains a diverse range of materials with varying reflectance properties that span large surfaces, providing sufficient data points for reasonable estimates. In contrast, Dataset 4 predominantly features similar materials, resulting in limited data per segment, which negatively impacts estimation quality and diminishes the benefits of material-specific AOI compensation. Additionally, Dataset 4 includes highly reflective surfaces, but the segmentation algorithm is unable to distinguish them as separate semantic classes. For example, the road class combines asphalt and road markings despite their distinct radiometric behaviors. This likely explains why local radiometric calibration noticeably underperforms in this case.

These observations highlight two key challenges: (i) the efficacy and robustness of our global compensation method and (ii) the difficulty of automatically estimating material-dependent AOI compensation functions.

Fig. 5 illustrates an example of material-dependent AOI compensation functions for four selected segments for the instance segmentation case of Dataset 2. These segments represent structures such as buildings, roads, and light poles, the latter are metallic and exhibit specular reflectance characteristics (see Fig. 6). The AOI functions of the road and the light poles are truncated due to high noise levels where insufficient data is available. The variability of the functions emphasizes the importance of segmentation and compensation for individual materials.

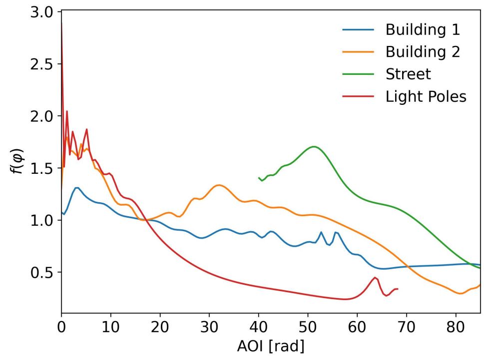

Figure 5. Estimated material-dependent AOI functions for four selected segments in Dataset 2.

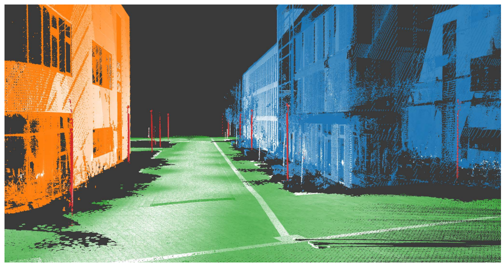

Figure 6. Instance segmentation with the following segments: blue: building 1, orange: building 2, green: street, red: light poles. The segments are saturated with the raw intensity.

Enhancing the material segmentation algorithm could further improve the results of the local methods. This can be achieved by incorporating the globally compensated $I^s_{\mathrm{MCI},j,k}$ values as additional information. We demonstrate this in the example of segmenting sinter in the retaining wall of Dataset 4. Here, the sinter can be effectively segmented by applying a simple threshold to the $I^s_{\mathrm{MCI},j,k}$ values (see Fig. 7c). In contrast, using raw intensities makes such segmentation unfeasible. In this case, not all sinter could be identified with a high threshold, while with a low threshold, the lower part of the wall would be incorrectly classified as sinter (see Fig. 7a and 7b).

We see this as a demonstration of how the classification of materials can significantly benefit from $I^s_{\mathrm{MCI},j,k}$ values. However, this creates a recursive challenge: Segmentation of different materials using intensities requires accurate radiometric compensation, and accurate compensation, in the case of the locally adapted $f^{\mathrm{mat}_j}_{\varphi_0}(\varphi_{j,k})$, relies on correct material segmentation. This issue could be solved with an iterative approach. First, $I^s_{\mathrm{MCI},j,k}$ values could be estimated globally, enabling segmentation based on these values. Subsequently, material-specific $I^s_{\mathrm{MCI},j,k}$ values could be calculated, which in turn, would refine the segmentation. This process could be repeated iteratively until convergence is achieved. However, the development of such an algorithm remains part of our future work.

6. Conclusion

This study adapts a previously developed in-situ radiometric calibration method for TLS intensity values, extending it to MLS data to compensate for measurement configuration (distance and angle of incidence, i.e., AOI). The method automatically estimates a distance compensation function for the entire dataset and an AOI compensation function estimated globally

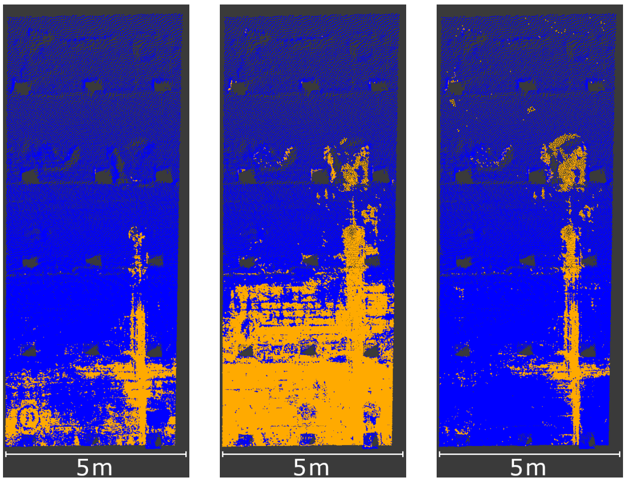

(a) (b) (c)

Figure 7. Part of the retaining wall in Dataset 4 as in Fig. 3. The point clouds are segmented into two parts to get the region with sinter (orange) and without (blue) based on the raw intensity and a high threshold (a), on the raw intensity and a low threshold (b) and on the $I^s_{\mathrm{MCI},j,k}$ values (c).

(for the entire dataset) or locally (per semantic class or individual instances). Using the estimated compensation functions, measurement configuration-independent intensities, $I^s_{\mathrm{MCI},j,k}$, can be computed and used for the downstream tasks with improved performance relative to original (raw) intensity values.

The applied method must account for varying radiometric properties across the scene. The global method leverages overlapping regions to optionally normalize for reflectance, while the local method compensates for these variations by estimating separate functions for each segment. As a result, the global method performs better in datasets with overlapping scan lines, whereas the local approach is better suited in datasets with a high diversity of surface and material types. Since the local method estimates an individual AOI compensation function for each segment, accurate segmentation based on material properties is crucial to ensure proper modeling.

To overcome the necessity of manual separation of the surfaces of different materials and, thus, different radiometric properties, in the case of the local compensation method, we used a semantic segmentation approach for 3d point clouds based on an in-built machine-learning model within Leica's Cyclone 3DR software. However, since this algorithm is designed for semantic rather than material-related segmentation, the obtained classes served only as proxies for the surfaces with common radiometric properties (typically, one semantic class contains multiple distinct materials). Additionally, separating a limited amount of data into locally adapted estimation data sets imposes constraints on the quality of such locally estimated AOI compensation functions. Hence, fully benefiting from this local approach, these limitations have to be tackled either to improve through integrating better-suited segmentation methods or smarter incorporation of prior knowledge for the used AOI functions.

Finally, by comparing the distance compensation functions estimated for scanners of the same type, we observed that these functions can be jointly estimated, which can be relevant for multi-scanner systems. In conclusion, the proposed method reduces the influence of the measurement configuration in MLS intensity data. The derived $I^s_{\mathrm{MCI},j,k}$ are particularly advantageous for tasks such as segmentation, as demonstrated in a simplified classification case.

Acknowledgments

This research was supported by the ETH Research Grant "Protecting Sandstone Monuments". We would like to thank Professor Heiner Kuhlmann's group at the University of Bonn, with special thanks to Felix Esser, for their contribution in providing Datasets 1–3. We are also grateful to Professor Werner Lienhart's group at the University of Graz, especially Slaven Kalenjuk, for providing Dataset 4.

References

Ester, M., Kriegel, H.-P., Sander, J., Xu, X., 1996. A density-based algorithm for discovering clusters in large spatial databases with noise. *Proceedings of the Second International Conference on Knowledge Discovery and Data Mining*, KDD'96, AAAI Press, 226–231.

Han, Y., Salido-Monzú, D., Wieser, A., 2022. Comb-based multispectral LiDAR providing reflectance and distance spectra. *Opt. Express*, 30(23), 42362–42375.

Harintaka, H., Wijaya, C., 2024. Improved deep learning segmentation of outdoor point clouds with different sampling strategies and using intensities. *Open Geosciences*, 16(1), 20220611.

Heinz, E., 2021. Beiträge zur Kalibrierung und Evaluierung von Multisensorsystemen für kinematisches Laserscanning. PhD thesis, Rheinische Friedrich-Wilhelms-Universität Bonn.

Jelalian, A., 1992. *Laser Radar Systems*. Artech House.

Jin, J., Verbeurgt, J., De Sloover, L., Stal, C., Deruyter, G., Montreuil, A.-L., Vos, S., De Maeyer, P., De Wulf, A., 2021. Support vector regression for high-resolution beach surface moisture estimation from terrestrial LiDAR intensity data. *International Journal of Applied Earth Observation and Geoinformation*, 102, 102458.

Kaasalainen, S., Ahokas, E., Hyyppa, J., Suomalainen, J., 2005. Study of surface brightness from backscattered laser intensity: calibration of laser data. *IEEE Geoscience and Remote Sensing Letters*, 2(3), 255-259.

Kaasalainen, S., Niittymaki, H., Krooks, A., Koch, K., Kaartinen, H., Vain, A., Hyyppä, H., 2010. Effect of Target Moisture on Laser Scanner Intensity. *IEEE Transactions on Geoscience and Remote Sensing*, 48(4), 2128–2136.

Kalenjuk, S., Lienhart, W., Rebhan, M. J., 2021. Processing of mobile laser scanning data for large-scale deformation monitoring of anchored retaining structures along highways. *Computer-Aided Civil and Infrastructure Engineering*, 36(6), 678–694.

Kashani, A., Olsen, M., Parrish, C., Wilson, N., 2015. A Review of LIDAR Radiometric Processing: From Ad Hoc Intensity Correction to Rigorous Radiometric Calibration. *Sensors*, 15(11), 28099–28128.

Laasch, H., Medic, T., Pfeifer, N., Wieser, A., 2025. Automatic in-situ radiometric calibration of TLS: Compensating distance and angle of incidence effects using overlapping scans. (In Review).

Li, X., Yu, R., Bi, T., Xu, L., 2024. A Traffic Sign Classification Method Using LiDAR Corrected Intensity and Geometric Feature. *IEEE Sensors Journal*, 24(7), 11796-11804.

Maru, M. B., Wang, Y., Kim, H., Yoon, H., Park, S., 2023. Improved building facade segmentation through digital twin-enabled RandLA-Net with empirical intensity correction model. *Journal of Building Engineering*, 78, 107520.

Pfeifer, N., Dorninger, P., Haring, A., Fan, H., 2007. Investigating terrestrial laser scanning intensity data: quality and functional relations. *8th Conference on Optical 3-D Measurement Techniques*, 328–337.

Pfeifer, N., Höfle, B., Briese, C., Rutzinger, M., Haring, A., 2008. Analysis of the backscattered energy in terrestrial laser scanning data. *International Archives of Photogrammetry, Remote Sensing and Spatial Information Sciences*, 37, 1045–1051.

Pfreundschuh, P., Oleynikova, H., Cadena, C., Siegwart, R., Andersson, O., 2024. Coin-lio: Complementary intensity-augmented lidar inertial odometry. *2024 IEEE International Conference on Robotics and Automation (ICRA)*, IEEE, 1730–1737.

Sanchiz-Viel, N., Bretagne, E., Mouaddib, E. M., Dassonvalle, P., 2021. Radiometric correction of laser scanning intensity data apllied for terrestrial laser scanning. *ISPRS Journal of Photogrammetry and Remote Sensing*, 172.

Tan, K., Chen, J., Zhang, W., Liu, K., Tao, P., Cheng, X., 2020. Estimation of soil surface water contents for intertidal mudflats using a near-infrared long-range terrestrial laser scanner. *ISPRS Journal of Photogrammetry and Remote Sensing*, 159, 129–139.

Viswanath, K., Jiang, P., Sujit, P., Saripalli, S., 2023. Off-road lidar intensity based semantic segmentation. *International Symposium on Experimental Robotics*, Springer, 608–617.